Numerical modelling of the extensional dynamics in elastoviscoplastic fluids

Journal of Non-Newtonian Fluid Mechanics 318 (2023) 105060

Contents lists available at ScienceDirect

Journal of Non-Newtonian Fluid Mechanics

journal homepage: www.elsevier.com/locate/jnnfm

Numerical modelling of the extensional dynamics in elastoviscoplastic fluids

Muhammed Abdulrazaq [a], Armin Shahmardi [b,*], Marco Edoardo Rosti [c], Luca Brandt [b,d]

[a] Fluids and Flows group, Department of Applied Physics, Eindhoven University of Technology, P.O. Box 513, 5600MB, Eindhoven, The Netherlands
[b] SeRC (Swedish e-Science Research Centre) and Flow, KTH, Department of Engineering Mechanics, SE-10044 Stockholm, Sweden
[c] Complex Fluids and Flows Unit, Okinawa Institute of Science and Technology Graduate University, 1919-1 Tancha, Onna-son, Okinawa 904-0495, Japan
[d] Department of Energy and Process Engineering, Norwegian University of Science and Technology (NTNU), Trondheim, Norway

ARTICLE INFO

Keywords:
Non-Newtonian fluid
Elastoviscoplastic fluid
Extensional rheology

ABSTRACT

The extensional dynamics of an elasto-viscoplastic (EVP) fluid is studied by means of numerical simulations modelling an experimental configuration. Specifically, we track the interface between the EVP material and the Newtonian medium using an algebraic volume of fluid method (MTHINC-VOF) and employ a fully Eulerian immersed boundary method (IBM) to model the motion of the piston responsible for the extension of the material. We investigate the role of different values of the yield stress, surface tension at the interface between the EVP material and the surrounding fluid, polymer viscosity ratio, and extension rates on the necking thickness of the material, extensional viscosity, and yielding of the material for two sets of parameter with low and high elasticity. The results of the simulations reveal that when the yield stress of the EVP material is much larger than the viscous stresses, the material undergoes an elastic deformation, regardless of the selected values of the extension rate, interfacial forces, and viscosity ratio. Moreover, by increasing the ratio of the polymeric viscosity to the total viscosity of the system, the EVP material produces stronger strain hardening and reaches the minimum resolvable width sooner. Specific and novel to our study, we show that interfacial forces cannot be ignored when the surface tension coefficient is such that a Capillary number based on the extensional rate is of order 1. For large values of the surface tension coefficient, the EVP material fails sooner, with a clear deviation from the exponential reduction in the neck thickness. Moreover, our results suggest that the role of the yield stress value on the dynamics of the material is more pronounced at lower elasticity.

1. Introduction

Researchers in fluid mechanics have soon identified the need to consider fluids for which the stress tensor is not linearly proportional to the strain rate and memory effects become important. Indeed, in many industrial and biological applications, working fluids exhibit a more complex behaviour and are categorised as non-Newtonian. Blood flow in biological tissues, liquid foams, polymer solutions and hot metal forming in industry and mudslides, meteoric and tectonic dynamics of the earth in geological fluid dynamics [1], food processing [2], film blowing, drag reduction, lubrication, extrusion and fibre spinning [3], ink jet printing [4], atomisation of fertilisers and pesticides and electro-spinning processes [5] are examples of the importance of non-Newtonian fluids.

The presence of a microstructure may cause non-Newtonian fluids to exhibit variable viscosity and elastic and/or plastic behaviour, i.e. viscoelastic materials and yield stress and viscoplastic fluids. Some materials may show both plasticity and elasticity, the so-called elasto-viscoplastic materials (hereafter referred to as EVP materials) [6]; if the applied stress is less than a threshold value (yield stress) the material remains solid and undergoes elastic deformations due to the applied shear. The same material, however, starts flowing if the applied stress exceeds the yield stress [6,7].

Several studies in the past have separately considered viscoelastic and viscoplastic fluids. Recent observations, however, have proved the existence of material deformation below the yield stress as well as extensibility of some yield stress materials. Carbopol has been shown to display elastoviscoplastic properties [8]. Bamforth et al. [9] ascribed the discrepancies in the comparison between experiments in Kaolin (a yield stress fluid) and computational results to the possibility of deformation below the critical (yield) stress. Furthermore, phenomena such as the fore-and-aft asymmetry and negative wake behind a sphere observed experimentally for the flow of yield stress fluids have been attributed to the elasticity of the yield stress materials [10]. Nelson

* Corresponding author.
E-mail address: arminsh@mech.kth.se (A. Shahmardi).

https://doi.org/10.1016/j.jnnfm.2023.105060
Received 19 May 2022; Received in revised form 21 April 2023; Accepted 26 April 2023
Available online 29 April 2023

et al. [2] have recently documented high extensibility in yield stress materials. These studies all point to the fact that yield stress fluids inevitably have intrinsic elastic properties which should be considered.

These observations motivated several attempts to introduce mathematical descriptions of EVP fluids. Yoshimura et al. [11] extracted the material rheology under large amplitude oscillatory shear (LAOS) of an elastic Bingham model to match experiments. The same base model was later extended by Doraiswamy et al. [12] to include a Cox–Merz rule. Furthermore, Sollich et al. [13] introduced a probabilistic method to describe some of the features of EVP materials. Saramito [7] developed a tensorial constitutive model wherein the material behaves as a Kelvin–Voigt solid before a critical stress is reached and as an Oldroyd-B viscoelastic fluid above the critical stress. To account for shear thinning (e.g. Carbopol [8] and liquid foams [14]) and the less common shear thickening observed in some materials after yield, Saramito [15] improved his earlier model to predict a Kelvin–Voigt solid before yielding and a non-linear, viscoelastic, Herschel–Bulkley fluid after yielding. Unlike previous models for elastoviscoplasticity, the models in [7,15] are thermodynamically admissible. Additionally, they predict a smoother behaviour as the material transitions through yielding. Benito et al. [16] also presented a tensorial, non-linear Bingham model for EVP foams and emulsions based on the evolution of a so called "stored deformation tensor". This model predicts the deformation in the elastic regime before the occurrence of plastic creep and viscous flow at higher applied stresses. Borrowing ideas from solid mechanics, Dimitriou and McKinley [17] introduced an EVP model which accounts for complex rheological responses like kinematic hardening and thixotropy. In this paper, we adopt the model from Saramito [7], which was proved to be suitable for numerical simulations, see e.g. [18–20]

From a practical point of view, a primary consideration is how to measure the properties of these complex EVP materials. Over the years, the extensional filament stretching procedure [21,22] has turned out to be effective in extracting rheological properties of complex fluids. Consequently, both experimental and (few) numerical efforts have focused on the dynamics of filament stretching in non-Newtonian fluids. Among those, Valette et al. studied fast stretching of fluid filaments using numerical simulations and compared the results with experiments [23]. Their results show the role of Newtonian viscosity, surface tension and Bingham yield stress on the deformation of the filament and the formation of drops or broken threads.

Unlike the case of shear flows (dictated by a linear input [22]), extensional flows are dictated by a non-linear exponential input and can therefore impose more stringent kinematic conditions on the flow. As a result, several non-linear features (like extensional strain hardening) only become apparent with an extensional procedure [24,25]. It should also be considered that extensional flows present themselves as better candidates to reveal the physics of flexible macromolecules and the orientation of rigid molecules [22].

Considering the limitations often faced by experimentalists where the parameter range is usually restricted by the test material, numerical simulations offer a certain flexibility in the parameter selection and the possibility of performing more detailed analyses. For viscoelastic fluids, early numerical efforts to model extensional flows used either an Eulerian finite-element method for differential viscoelastic constitutive equations (e.g. [21,26]), the Lagrangian finite-element approach for integral constitutive equations (e.g [27]) or the boundary-element method (e.g. [28]). Here, we borrow the idea of [29] and adjust their method to model a moving wall with interface tracking to define the material deformation. The proposed model is fully Eulerian, hence requires less computational resources and facilitates the code parallelisation.

Past attempts to numerically simulate filament stretching in yield stress fluids include the work by Balmforth et al. [9], who modelled the extensional and thinning dynamics of yield stress bridges using the slender filament approach based on the Herschel–Bulkley constitutive equation, and Dimakopoulos et al. [30], who developed a penalised augmented Lagrangian algorithm for a yield stress fluid which compared favourably with the simulations from Balmforth et al. [9]. Also following this work, Moschopoulos et al. [31] performed simulation of linearly extending yield stress fluids using the half length model.

In this context, the objective of the present work is twofold. On one hand we wish to establish a numerical framework for high-fidelity realistic simulations of extensional flows where different constitutive relations could be tested against experimental data. Indeed, extensional flows reveal more easily the nonlinear material dynamics and present therefore a more stringent test for any theoretical modelling. Of particular interest here, the rheological modelling of elastoviscoplasticity is challenging due to nonlinearities and complex constitutive equations [32,33]. On the other hand, we hope the present simulations contribute to fill some gaps in our current understanding of the material behaviour, those mainly due to simplifying assumptions in current theoretical investigations. In detail, our work aims to investigate the combined effect of capillarity, elasticity, inertia, plasticity and viscosity on the filament stretching by means of numerical simulations of the Saramito model, with minimum assumptions in terms of physical properties. By doing this, we wish to extend the current discussion and analysis of the extensional dynamics of complex fluids from *visco-elasto-capillary* [5] to *visco-elasto-plasto-capillary*.

The paper is organised as follows. In Section 2, we introduce and describe the governing equations whereas the scheme and algorithm used for their numerical solution are introduced in Section 3. We present the physical configuration in Section 4 and discuss the results of our numerical simulations in Section 5. We conclude the paper by summarising the major findings in Section 6.

2. Governing equations

We will simulate the stretching of an EVP material in a second fluid. To track the interface between the EVP material and the Newtonian medium and computing the interaction forces between the two phases in the system, we employ a volume of fluid method. To do so, we define an indicator (or colour) function which is 1 inside the EVP and zero otherwise. We denote the indicator function by H and update it by solving the following advection equation [34]:

$$\frac{\partial \phi}{\partial t} + \frac{\partial u_i H}{\partial x_i} = \phi \frac{\partial u_i}{\partial x_i}, \tag{1}$$

where ϕ is the averaged value of the indicator function in each cell, and u_i represents the velocity vector.

The fluid motion is governed by the conservation of mass and momentum:

$$\begin{aligned} \frac{\partial u_i}{\partial x_i} &= 0, \\ \frac{\partial \rho u_i}{\partial t} + \frac{\partial \rho u_i u_j}{\partial x_j} &= \frac{\partial \sigma_{ij}}{\partial x_j} + f_{\sigma_i} + f_{I_i}, \end{aligned} \tag{2}$$

where f_{I_i} is the immersed-boundary force (discussed later in the next section), f_{σ_i} represents the surface tension forces, and σ_{ij} is the Cauchy stress tensor:

$$\sigma_{ij} = -P\delta_{ij} + 2\mu e_{ij} + \tau_{ij}. \tag{3}$$

Here P is the pressure, δ is the Kronecker delta, μ the dynamic viscosity and e_{ij} denotes the strain rate tensor:

$$e_{ij} = \frac{1}{2}\left(\frac{\partial u_i}{\partial x_j} + \frac{\partial u_j}{\partial x_i}\right). \tag{4}$$

In Eq. (3), τ_{ij} represents the viscoelastic stress tensor which models the non-Newtonian fluid characteristics. We employ the constitutive equation proposed by Saramito [35] to model the non-Newtonian stress in the EVP material. In this model, if the stress is below the yield stress (τ_y), the fluid element only undergoes recoverable Kelvin–Voigt viscoelastic deformation; however, if the stress exceeds the yield

stress, the model reduces to the Oldroyd-B viscoelastic model. The components of the non-Newtonian stress tensor are therefore governed by the following transport equation:

$$\lambda\left(\frac{\partial\tau_{ij}}{\partial t}+u_k\frac{\partial\tau_{ij}}{\partial x_k}-\tau_{kj}\frac{\partial u_i}{\partial x_k}-\tau_{ik}\frac{\partial u_j}{\partial x_k}\right)+max\left(0,\frac{|\tau_d|-\tau_y}{|\tau_d|}\right)\tau_{ij}=2\mu_p e_{ij}, \tag{5}$$

where λ and μ_p represent the relaxation time and an additional viscosity. In Eq. (5), $|\tau_d|$ is the second invariant of the deviatoric part of the non-Newtonian stress tensor $|\tau_d|=\sqrt{0.5\,\tau_{ij}^d\tau_{ij}^d}$.

3. Numerical method

We solve the system of equations introduced above on a staggered mesh: the velocity components are defined at the faces whereas all the other variables are defined at the cell centre. All the spatial derivatives are discretised using second-order finite differences except that, for numerical stability purposes, the advection term in the transport equation for the non-Newtonian stresses (see Eq. (5)) is discretised using a fifth-order WENO scheme; nevertheless the spatial order of convergence is eventually quadratic because it is limited by the 2nd order finite differences used for the remaining terms. The different equations are advanced in time using the second order Adams–Bashforth scheme. Finally, we use a fractional-step method to impose the incompressibility constraint on two-fluid system, following the procedure suggested in Dodd and Ferrante [36].

To reconstruct the interface between the EVP and the external Newtonian fluid, among different VOF models, we employ the multidimensional tangent of hyperbola for interface capturing method (hereafter will be referred to as MTHINC-VOF). The method was originally proposed by [34] and extended to multiple dimensions in [37]. In the MTHINC-VOF model, the indicator function (H) is approximated as follows:

$$H(\boldsymbol{x},t)\approx\tilde{H}\left(x_i\right)=\frac{1}{2}\left[1+\tanh\left(\beta\left(P_n\left(x_i\right)+d\right)\right)\right], \tag{6}$$

where x_i are the coordinates in space, β is a sharpness parameter, and d is a normalisation parameter. $P_n(x_i)$ is a quadratic function of the coordinate vector. We define the local normal vector (n_i) and the six values of the curvature tensor (R_{ij}) as [38]:

$$\begin{aligned} n_i &= \frac{1}{|\frac{\partial\phi}{\partial x_i}|}\frac{\partial\phi}{\partial x_i} \\ R_{ij} &= \frac{1}{2}\left(\frac{\partial n_i}{\partial x_j}+\frac{\partial n_j}{\partial x_i}\right). \end{aligned} \tag{7}$$

The normalisation parameter (d) is computed to satisfy the following constraint:

$$\int_0^1\int_0^1\int_0^1\tilde{H}\,dX_1dX_2dX_3=\phi. \tag{8}$$

Once the indicator function H and its averaged value at each cell ϕ are updated by solving Eq. (1), we compute the surface tension forces acting on the interface using the continuum surface force (CSF) model [39]:

$$f_{\sigma_i}=-\sigma\frac{\partial n_j}{\partial x_j}\frac{\partial\phi}{\partial x_i}. \tag{9}$$

Note finally that the solvent viscosity, μ, and the density, ρ, vary between ρ_1 and μ_1 inside the EVP fluid to ρ_2 and μ_2 in the Newtonian medium through a linear interpolation based on the local value of the function ϕ [38].

The EVP material is extended by pulling a piston attached to its top side. To model the piston, we use the immersed-boundary model (IBM) proposed by Kajishima et al. [40] and combine it with the selected interface tracking approach (MTHINC-VOF) by adjusting the method proposed in [29]. We define the local volume fraction (γ) as the fraction of volume of the computational cell occupied by the piston; hence, the volume fraction is zero for all the numerical cells in the fluids and unity for the cells entirely located inside the piston. Kajishima et al. suggested to calculate the IBM force, f_{I_i}, used in the momentum equations as

$$\begin{aligned} f_{I_i} &= \gamma\frac{u_{p_i}-u_i^*}{\Delta t} \\ u_i^{**} &= u_i^*+\Delta t f_{I_i} \end{aligned} \tag{10}$$

where u_{p_i} is the piston velocity (computed to satisfy the prescribed extension rate), u_i^* is the typical prediction velocity in any fractional step algorithm, and u_i^{**} is defined as the second prediction velocity using Eq. (10). The present implementation of an EVP fluid and of the VOF method has been extensively validated in several previous works, see e.g. [32,38,41].

It is worth to recall that the type and value of boundary condition for the volume fraction ϕ changes the shape of the material at the wall, and thus partially affects the extensional dynamics where the boundary condition controls the wettability of the solid surface. Here, however, we will not consider variations of the contact angle. In the employed Immersed Boundary framework, we only prescribe the velocity boundary condition at the solid wall and let the coupled system of equations (Naviers Stokes Eq. (2) and VOF transport (1)) control the contact dynamics at the wall via a balance between surface tension and advection. Effectively, the interface behaves as a free surface near the end plates.

4. Simulation setup

Fig. 1(a) illustrates the setup used in all the simulations. The computation domain (light grey area in Fig. 1a) has size $[X_1,X_2]\times[4R_0,12R_0]$, where R_0 is the initial width of the EVP sample used as reference lenght; the origin of the adopted Cartesian coordinate system is on the left bottom of the numerical domain. The two-dimensional sheet of the EVP material (coloured in blue) is initially placed between a solid substrate and a solid piston (both are represented in dark grey in Figs. 1(a) to (d). The initial height and width are chosen to ensure that the initial aspect ratio is unity, i.e. both equal to R_0. This value has been recommended and specified to be the optimal aspect ratio for th sample stretching procedures [21,27,42]. The piston moves upward with a prescribed velocity corresponding to the desired extension rate $\dot{\epsilon}$:

$$u_p=\frac{dL}{dt},\qquad L(t)=R_0e^{\dot{\epsilon}t}. \tag{11}$$

The position of the piston is represented in Fig. 1(e) versus time for the three values of the extension rate studied here. During the extension, we monitor the evolution of the minimum thickness of the EVP material, denoted by $R(t)$, see Fig. 1(c), until the sample breaks (panel 1d). The non-Newtonian contribution of the extensional viscosity is calculated from the averaged value (along the X_1 direction) of the normal stress difference at the wall-normal location of minimum thickness of the EVP sample, denoted X_{2_m} in Fig. 1c:

$$\mu_E^+\left(\dot{\epsilon_0},t\right)=\left[\tau_{11}\left(X_{2_m},t\right)-\tau_{22}\left(X_{2_m},t\right)\right]/\dot{\epsilon_0}, \tag{12}$$

where $\dot{\epsilon_0}$ is the initially imposed extension rate and the square bracket indicate the spatial averaging. A periodic boundary condition is imposed for all the variables on the left and right boundaries of the domain, while the bottom and the top boundaries are modelled as solid walls with no-slip and impermeability boundary conditions for the velocity components and Neumann boundary conditions for the pressure. We define the initial length of the EVP sample, R_0, the inverse of the extension rate ($1/\dot{\epsilon}$), and $R_0\dot{\epsilon}$ as the reference length, time, and velocity. The density of the EVP material is considered as the reference density ($\rho_0=\rho_1$) and the total viscosity of the EVP, i.e. the summation of the Newtonian and polymeric viscosity, is assumed as the reference viscosity, $\mu_0=\mu_1+\mu_p$. Using these reference values, we define the

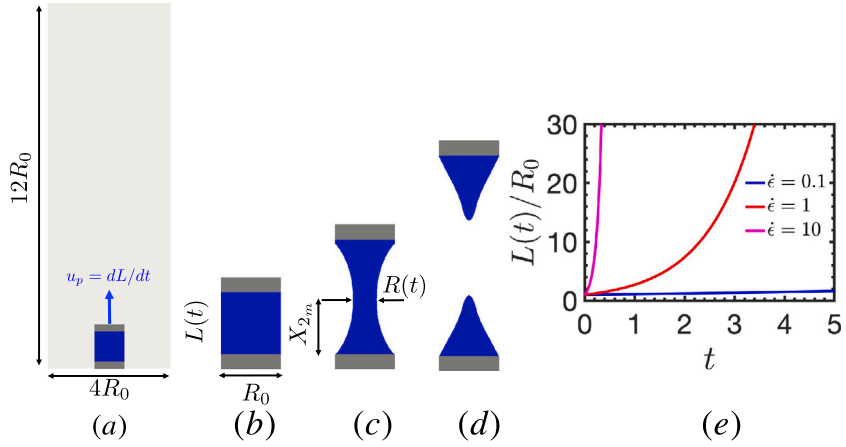

Fig. 1. Schematic of the simulation setup. The sample, a square of edge R_0, is placed on a solid substrate and attached to a piston moving upwards with velocity u_p, defining an extension rate $\dot{\epsilon}$. The computational domain has dimensions $4R_0 \times 12R_0$ in the wall-parallel and stretching directions.

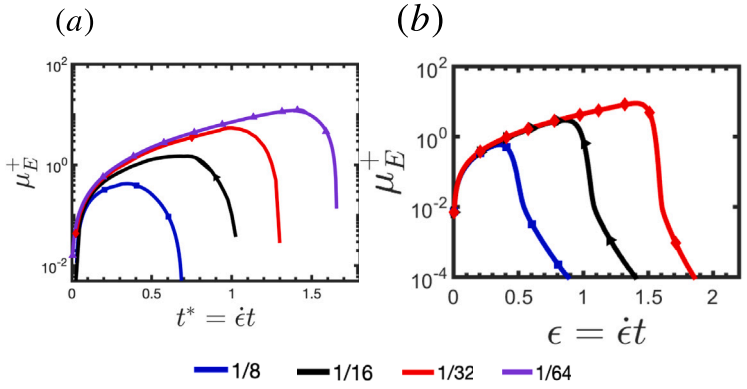

Fig. 2. Extensional viscosity versus the material extension, $t^* = \dot{\epsilon}t$, for varying grid sizes i.e. $\Delta x = 1/8, 1/16, 1/32, 1/64$. The simulations are performed for two sets of the governing physical parameters. For the results on the left, we set $Wi = 1.0, Re = 0.01, Bi = 0, Ca = \infty, \kappa_\rho = 1, \kappa_\mu = 1, \alpha = 0.9$ whereas for the configuration on the right, $Wi = 1.0, Re = 0.01, Bi = 1, Ca = 100, \kappa_\rho = 10^2, \kappa_\mu = 10^4, \alpha = 0.5$.

Weissenberg number (Wi), the Reynolds number (Re), the Bingham number (Bi), and capillary number (Ca) as follows:

$$Wi = \lambda\dot{\epsilon}, \qquad Re = \frac{\rho_0 \dot{\epsilon} R_0^2}{\mu_0}, \qquad Bi = \frac{\tau_y}{\mu_0 \dot{\epsilon}}, \qquad Ca = \frac{\mu_0 \dot{\epsilon} R_0}{\sigma}. \tag{13}$$

Furthermore, we define κ_ρ and κ_μ as the ratio of density and viscosity of the EVP material and the external Newtonian fluid, and the viscosity ratio $\alpha = \mu_p/(\mu_1 + \mu_p)$.

4.1. Grid independence studies

To determine a suitable mesh size, we first perform simulations for a flow with $Wi = 1.0, Re = 0.01, Bi = 0, Ca = \infty, \kappa_\rho = 1, \kappa_\mu = 1$, and $\alpha = 0.9$ using different grid sizes, namely $\Delta x = 1/8, 1/16, 1/32, 1/64$. The extensional viscosity $\mu_E^+(\dot{\epsilon_0}, t)$ at the section of minimum width of the EVP material is displayed in Fig. 2a for the different resolutions. Because we use a fixed (Eulerian) mesh, we can resolve the sample thickness up to the numerical grid size, and cannot reproduce an infinite thinning of the EVP material before the break-up. In other words, the smaller the grid size, the later the EVP sample breaks. We therefore restrict our grid convergence analysis to the initial part of the thinning process. According to Fig. 2a, the difference in extensional viscosity at the late stages, i.e. before the sample breakup, is reasonably small between the grids of size 1/32 and 1/64. To confirm the choice of the resolution 1/32, we investigate the grid convergence for a second flow, characterised by $Wi = 1.0, Re = 0.01, Bi = 1, Ca = 100, \kappa_\rho = 10^2, \kappa_\mu = 10^4$, and $\alpha = 0.5$. Our results, (see Fig. 2b), show that the numerical solution converges with mesh size 1/32 also in this case. Hence, the resolution $\Delta x = 1/32$ is used to obtain the results discussed below, which provides good results within a reasonable amount of computational time, allowing us to perform a full parametric study. Note that, in the employed algebraic Volume of Fluid method, the variation of the averaged indicator function, ϕ, is roughly restricted to two numerical cells. Thus, considering the selected grid size of $\Delta x = 1/32$, simulation results are not reliable when the width of the filament decrease to values below 2/32 ($R_{min} < 0.0625$), corresponding to a minimum physical value $R_{min}/R_0 = 0.03125$. Hereafter, we refer to this limit as the minimum resolvable width of the material.

5. Results and discussion

We define as main reference the case with $Wi = 1.0$, $Re = 0.01$, $Ca = 100$, $Bi = 1$, $\kappa_\rho = 10^2$, $\kappa_\mu = 10^4$, and $\alpha = 0.5$. It is worth to mention that typical values for density and viscosity ratios between an EVP material and air in experiments are $\kappa_\rho \approx 10^3$, $\kappa_\mu \approx 10^5$. Given the large parameter space, we selected a reference case with non-negligible elasticity and yield stress, and a surrounding fluid with significantly lower viscosity and density. A significant contribution of elasticity to the dynamics has been chosen to also compare with the several results in literature for viscoelastic materials. Selecting larger the values of

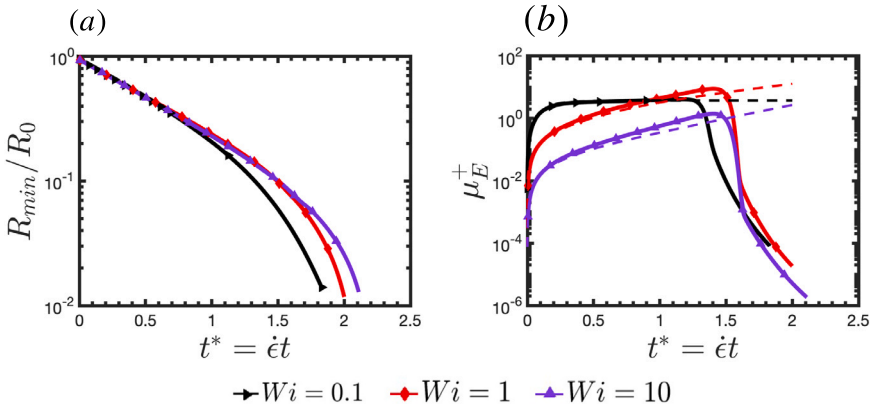

Fig. 3. (a) Normalised width and (b) extensional viscosity at the minimum radial section versus the non-dimensional time (or instantaneous extension) t^* for different Weissenberg numbers: $Wi = \dot{\epsilon}\lambda \in [0.1, 1, 10]$. The other parameters are: $Bi = 1.0, Ca = 100, Re = 0.01, \alpha = 0.5, \kappa_\rho = 10^2$ and $\kappa_\mu = 10^4$. The dashed lines represent the analytical solution of Saramito's model with corresponding colour for the corresponding cases.

viscosity or density ratios would require a smaller time step and make the simulations much more expensive. To be able to span a wide range of the governing parameters, we need therefore a trade-off between the choice of the density and viscosity ratios, κ_ρ and κ_μ, and the number of simulation cases.

To disentangle the effect of changing the yield stress (τ_y), surface tension coefficient (σ), extension rate ($\dot{\epsilon}$), and viscosity ratio, in the presence of all other physics, we will keep all the parameters as in the reference case and change only one of them at a time. In addition, to focus on the extensional dynamics at lower elasticity, approaching the limit of viscoplastic materials, we will also vary the yield stress (τ_y) and the surface tension coefficient (σ), for a second setup with $Wi = 0.01$, $Re = 0.01$, $\kappa_\rho = 10^2$, $\kappa_\mu = 10^4$, and $\alpha = 0.5$. Below, we present the effect of each parameter in separate subsections.

For our analysis, we will examine two (normalised) measures: (i) $R_{min}(t)/R_0$ the ratio between the minimal material width at time t and the initial width of the sample; (ii) the transient extensional viscosity at the minimum cross-section: $\mu_E^+(t) = [\tau_{11} - \tau_{22}]/\dot{\epsilon}_0$ where $[\tau_{11} - \tau_{22}]$ is the normal stress difference, averaged along the X_1 axis, at the sample minimum width. Note that, the sharp interface limit between the EVP material and the surrounding fluid is numerically captured by the curve $\phi = 0.5$

5.1. Effects of different values of the Weissenberg number

The time scale of the extensional process is determined by the extension rate $\dot{\epsilon}$, normalised here with the polymer relaxation time to give the Weissenberg number, Wi. When inertia is negligible, the dynamics change with the ratio between the imposed extensional time scale and the polymer relaxation. The ratio of these two time scales is one of the most important parameters dictating the dynamics of the sample stretching.

The change in width of the sample (smallest thickness of the EVP material as defined in Fig. 1c), and the extensional viscosity are shown versus the non-dimensional instantaneous extension (alternatively non-dimensional time, t^*) in Fig. 3 together with the analytical prediction for the extensional viscosity obtained from Saramito's model in the limit of density ratio $\kappa_\rho = 1$ and no surface tension ($Ca \to \infty$) for three values of the Weissenberg number, i.e. 0.1, 1 and 10. We note first that the extensional viscosity reaches its peak value at a lower extension for the case $Wi = 0.1$. As the polymer relaxation is faster than the imposed extension rate when $Wi < 1$, the extensional viscosity attains a constant value, a "steady state" behaviour, before the material reaches its minimum resolvable width, see panel b of the figure. For large values of Wi, on the contrary, the extensional viscosity increases until the sample width reaches the minimum resolvable value. The results suggest that the material stretches following the imposed extension with a certain delay at high Wi; the larger delay at the highest value of Wi under investigation explains the reduced value of the internal stresses (and of the extensional viscosity), while the geometry of the two samples is similar for $Wi = 1$ and $Wi = 10$, see the evolution of R_{min}/R_0 in panel (a) of Fig. 3.

We recall that, for the Saramito model considered here, the stress increases without bound under extension when $Wi \geq 0.5$, the so called "extensional catastrophe/coil-stretch transition" [21,24,43]. The fact that the material can extend indefinitely without failure is an artefact of the Oldroyd-B model, as also confirmed by numerical simulations of viscoelastic elements (e.g. [21,24]). Even though the Saramito model is an extension of the Oldroyd-B model, the sample will eventually break in a numerical simulation at finite resolution, as in the viscoelastic case in Ref. [21,24] (note that, as highlighted earlier, we cannot rely on the quantitative results when $R_{min}/R_0 < 0.03125$). Nevertheless, at higher extension rates ($Wi = 1$ and $Wi = 10$), the model shows that the stretching sample becomes thin quite rapidly and reaches the minimum resolvable width of the material after attaining a maximum of the extensional viscosity, as opposed to the case of lower extension rate where we observe a more gradual decrease of the extensional viscosity after its peak. As emphasised earlier, the infinite extensibility of the Oldroyd B model explains why the analytic solutions extend to infinitely large times, see Fig. 3.

To complement these observations, we present visualisations of the sample at two extension rates, i.e. two values of Wi, in Fig. 4. Note that in all the visualisations, the contour colours indicate the normal stress difference $[\tau_{11} - \tau_{22}]/\mu_0\dot{\epsilon}$ with corresponding values indicated by the side bars. To gain further insight on the physics of the extending sample, the unyielded region, i.e. the solid part of the EVP material, where the $|\tau_d| < \tau_y$ (see Eq. (5)), is depicted in red. First, we observe that the unyielded regions appear close to the end plates, in zones of low extensional stresses. However, because of the fast exponential dynamics of the high Wi case (or alternatively the slower material response), the middle part of the extending sample column is fully yielded, as observed for increased extensional rate in [9]. Surprisingly, we however observe a relatively large unyielded region near the plates. These regions are most likely just remaining from the initial state given the fast dynamics and/or slow material response at $Wi = 10$. For the low Wi case, the slower evolution of the EVP implies lower shear and extensional stresses, which explains why the unyielded regions near the plate are larger. Finally, we note that, although the regions

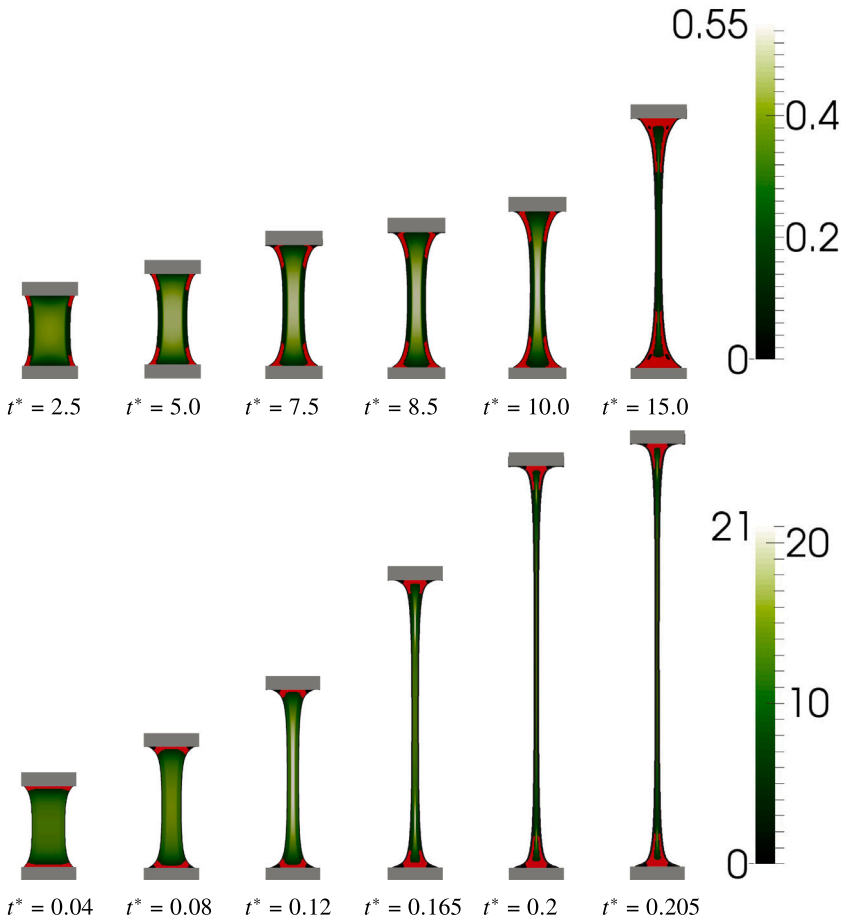

Fig. 4. Visualisation of the EVP sample stretching and evolution of the normal stress difference $\left[\tau_{11} - \tau_{22}\right]/\mu_0\dot{\epsilon}$ at (top) $Wi = 0.1$ and (bottom) $Wi = 10$ for the cases in Fig. 3. The red regions indicate the unyielded material. The other parameters are: $Ca = 100, Re = 0.01, Bi = 1.0, \alpha = 0.5, \kappa_\rho = 10^2$ and $\kappa_\mu = 10^4$.

close to the end plates have low extensional stresses, the shear stresses are relatively high due to the no-slip boundary condition [21]. The combination of high shear stresses and unyielded regions may seem contradictory. However, for an extending sample, the stresses mostly contributing to the value of the invariant $|\tau_d|$ are the tensile and not the shear stresses. Hence, higher extensional stresses lead to yielding at the midsection whereas higher-shear stresses may not necessarily induce yielding close to the walls.

5.2. Effects of different values of Bingham number

We next study the effect of the yield stress on the extensional dynamics of the EVP fluid. To this aim, we first examine results for four values of the Bingham number, namely $Bi = [0, 0.01, 1, 100]$ and other parameters as for the main reference case introduced above, when elasticity is not negligible. The two observables considered here are displayed in Figs. 5a and 5b.

First, we note in Fig. 5b that the simulation results are in good agreement with the analytical solution of Saramito's model before the material reaches its minimum numerically resolvable width (see dashed lines). Note that we expect a minor difference between the simulation results ($Ca = 100$) and the analytical solution due to absence of capillary effects and density contrast in the Saramito's model. The data also reveal a minimal dependence of the dynamics of extension on Bi even though the yield stress is varied over several order of magnitudes (from 0.01 to 100). This is more evident for the evolution of R_{min}/R_0 where the only visible effect occurs near the end of the extensional process. We also note that the shape of the different curves is similar, which points to similar underlying extensional dynamics, with peak values only weakly dependent on the yield stress value, τ_y. This similarity can be understood by considering the dominant role of Newtonian viscous diffusion at the relatively small value chosen for the viscosity ratio (α) and the large elasticity.

To examine the effect of different Bi on the extensional dynamics and focus on the plasticity effects, we report in panels c and d of Fig. 5 the results for three values of the Bingham number, namely $Bi = [0, 0.01, 1]$ for the second reference case where $Wi = 0.01$. As anticipated by the data at low elasticity in Fig. 3, the minimum sample width decreases faster in the limit of vanishing material elasticity, whereas the extensional viscosity attains a constant value because of the quick material response, a "steady state" value, before the material reaches its minimum resolvable width, which is more gradual than in the cases with $Wi = 1$ in panel b especially at low values of Bi. Interestingly, we observe now a clear dependence on the Bingham number: the extensional viscosity μ_E increases with Bi and the sample thinning (the decrease of R_{min}/R_0) is faster. The value of the extensional viscosity is larger than in the cases with $Wi = 1$ at early times while becomes smaller at the high extensions preceding rupture.

The evolution of the EVP sample for the two extreme values of the Bingham number under investigations for cases with $Wi = 1$ is shown

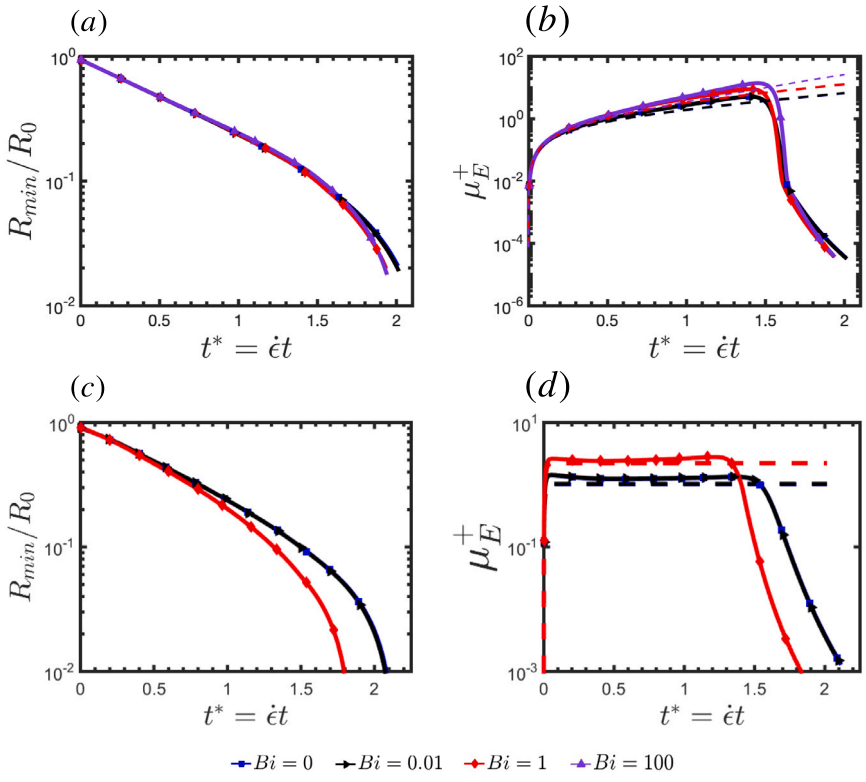

Fig. 5. Normalised width (left column) and extensional viscosity (right column) at the minimum radial section versus the non-dimensional time (or instantaneous extension) t^* for different values of the Bingham number, $Bi \in [0, 0.01, 1, 100]$ with $Wi = 1.0$, for the figures on the top row and $Wi = 0.01$, for the figures on the bottom. The other parameters are: $Ca = 100, Re = 0.01, \alpha = 0.5, \kappa_\rho = 10^2$ and $\kappa_\mu = 10^4$. The dashed lines represent the analytical results of Saramito's model for the corresponding cases.

in Fig. 6. As expected, the unyielded region is small when $Bi = 0.01$ and larger when $Bi = 100$. In particular, at high Bi, the material remains almost completely unyielded throughout the extensional process, and hence behaves as an "elastic solid". At lower values of the Bingham number instead, we observe that the fluid yielding begins from the middle of the sample and extends towards the end plates, see data for $Bi = 0.01$ in the figure, where one can find pockets of unyielded "elastic solid" close to the edges of the end plates while the rest of the EVP material behaves as a liquid. For this low Bi case, the unyielded regions at the corners of the plates at first slightly increase as the extension progresses (see image at time $t^* = 1.2$). The localisation of low stress at the corners described here (precursor to unyielded regions) was also observed in [21] for the extensional stress in viscoelastic sample. Here, however, we do not observe a thin boundary layer with high stresses at the midplane interface, which can be explained by the more homogeneous conditions due to a higher value of the sample initial aspect ratio.

We focus on the dynamics at low elasticity in Fig. 7. Consistent with the observations in Fig. 5(c) and 5(d), the visualisations suggest an important effect of the Bi at low extensibility, i.e, smaller valued of Wi. According to the top row in Fig. 7, small value of Bi, the material yields very fast and exhibit viscoelastic behaviour even at small extension rates. However, increasing the Bi number to 1, we observe an evolution of the unyielded regions. Right after starting the extension, the stress exceeds the yield stress everywhere in the material (except small regions at the interface) resulting in a fully viscoelastic behaviour of the sample. As the extension continues, owing to the fast response of the material at small Wi, the stress concentration shifts towards the central part of the sample where the necking happens. Therefore, the unyielded region appears to extend from the endplates (where the normal stresses are minor) towards the central part resulting in a triangular shape close to the endplates, as compared to the smooth and curved shape of the material at the endplates for the sample at lower Bi values.

Note that a similar "freezing" of the bottom regions, observed for both values of Wi considered here, was also reported for highly viscoplastic Bingham fluids [9] and the presence of unyielded regions close to the endplates has been previously reported for pure Bingham fluids under extension in [9,31].

Summarising, notwithstanding the large variation of Bi and the transition from mostly yielded to mostly unyielded flow, the differences in the overall behaviour are quite limited for the sample with $Wi = 1$. We believe that the weak dependence on Bi in the presence of significant elasticity may be ascribed to the fact that the yield stress parameter in the Saramito model is merely a "transition parameter" between two similar viscoelastic models. At low Bi, a "Saramito" fluid mainly exhibits the Oldroyd B viscoelastic behaviour, with constant shear viscosity, whereas the material behaves as a Kelvin–Voigt viscoelastic solid at higher values of Bi. Hence, a similar viscoelastic response is obtained here regardless of the value of the Bingham number chosen. Different is the case with a high value of the viscosity ratio, when the viscous response of the yielded Oldroyd B fluid differs from that of the Kelvin–Voigt viscoelastic solid. We will thus investigate the extensional dynamics for the extreme values of Bi under consideration ($Bi = 0.01, 100$) for low and high viscosity ratios ($\alpha = 0.1, 0.9$) in Section 5.4. In the limit of vanishing elasticity, on the contrary, we observe an increase of the extensional viscosity with Bi and a more rapid path to rupture.

5.3. Role of the capillary number

Before examining the effect of capillarity on the dynamics of an extending EVP sample, we note that previous numerical studies on

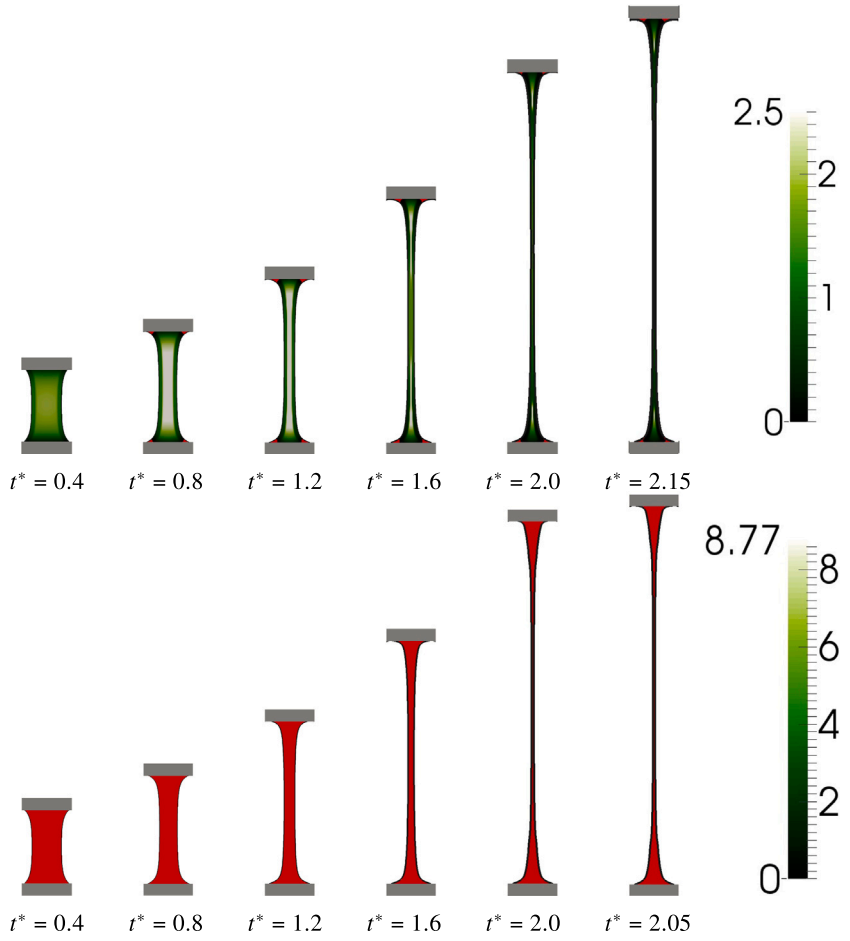

Fig. 6. Visualisation of the EVP sample stretching and evolution of the normal stress difference $\left[\tau_{11} - \tau_{22}\right] / \mu_0 \dot{\epsilon}$ at (top) $Bi = 0.01$ and (bottom) $Bi = 100$ with $Wi = 1$, see also data in the top row of Fig. 5. The red regions indicate the unyielded material.

non-Newtonian extensional flows (among others [24,25]) ignored the effect of surface tension. This is assumed to be important only in the final stages of necking in slowly extending fluids [24]. For very viscous or highly elastic non-Newtonian fluids, i.e. Wi and $Ca \gg 1$, where bulk stresses (viscous or elastic) dominate, the role of interfacial effects is expected to be minor [24,28]. In general, the axial stress in the sample increases when increasing capillarity [24,44]. This is clearly seen in the analytic expression for the extensional viscosity (obtained considering an ideal uniaxial flow) given in [45]. In addition, according to the analysis in [45], the effect of the surface tension is magnified when the width of the extending sample is small (at the later stages of the extending process) and when the change in the rate at which the width is reduced increases, supporting the assumptions mentioned above. To study the effect of the capillary number under more general conditions, we first consider five different values for Ca, namely $Ca \in [0.1, 1, 10, 100, \infty]$ for the main reference case, when the elasticity of the material is not negligible. The data pertaining the minimum normalised width and stress are presented in Fig. 8a and b. From the evolution of the width, we note that the effect of the capillary number is weak for values larger than 10. For lower values, i.e. $Ca \approx \mathcal{O}(1)$, when viscous and interfacial forces are comparable in magnitude, the width of the material decreases faster for larger values of the surface tension, though the behaviour is still initially exponential. The same trend is observed for the evolution of the extensional viscosity, see panel b of the same figure. Neglecting the surface tension forces would therefore lead to inaccurate predictions at low values of Ca, that is when the extension rate is relatively slow. It is also relevant to note that we use here a viscosity ratio $\alpha = 0.5$, meaning that the bulk elastic stresses are relatively modest, while they are stronger for higher values of α. Hence, we expect that lower values of Ca (or higher surface tension σ) will be needed to considerably affect the dynamics of the EVP material in highly viscoelastic fluids (large values of α). This observation is consistent with the assumption that capillary effects can be ignored in the case of high elastic stresses [24], unless the surface tension is particularly high.

In addition, our simulations reveal that the exponential extension of EVP material, corresponding to a straight line on a semilog plot, is not an accurate prediction when the Capillary number $Ca \lesssim 10$. This is clearly observed in Fig. 8a, where the deviation from the exponential reduction (a straight line) is seen for the lowest Capillary number considered. Note finally that we see a departure from the linear behaviour also in the absence of surface tension once close to minimum resolvable width of the material. This is however due to the fact that eventually the film ruptures because the sample cannot become indefinitely long at finite numerical resolution. This is also the case in experiments where infinite extension is prevented by other factors such as the nonlinear dynamics of realistic materials, and also the no-slip boundary condition at the end plates. Note that the Saramito model reduces to an Oldroyd-B model when the material yields resulting in an infinite extensibility, which is however not possible at finite numerical resolution.

As in Section 5.2, we further investigate the role of surface tension on the dynamics of an EVP material with lower $Wi = 0.01$. To do

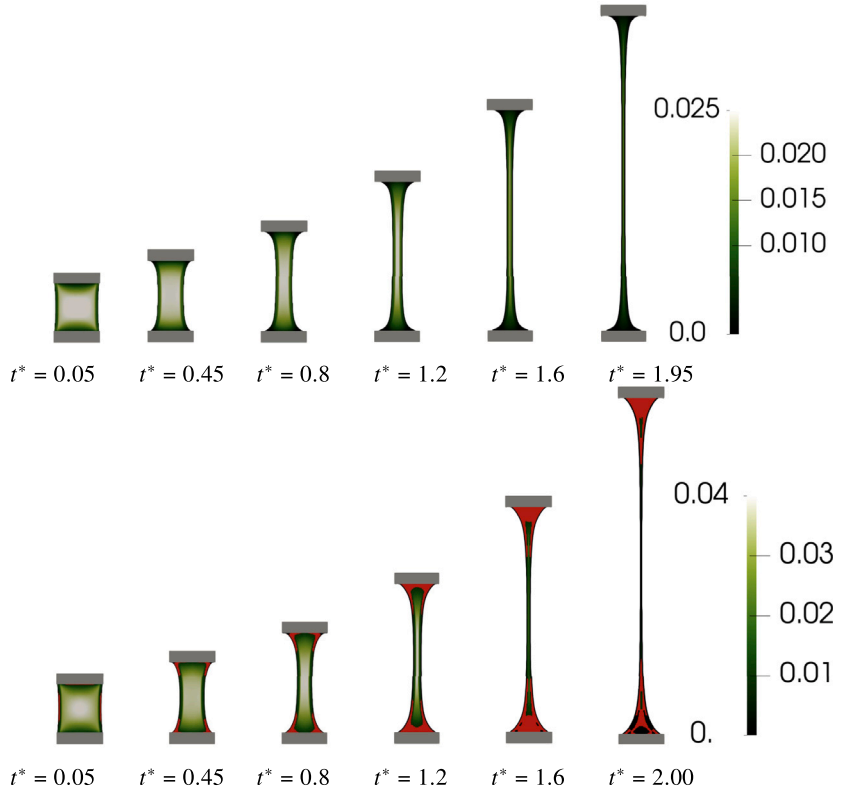

Fig. 7. Visualisation of the EVP sample stretching and evolution of the normal stress difference $\left[\tau_{11} - \tau_{22}\right] / \mu_0 \dot{\epsilon}$ at (top) $Bi = 0.01$ and (bottom) $Bi = 1$ with $Wi = 0.01$, see also data in the bottom row of Fig. 5. The red regions indicate the unyielded material.

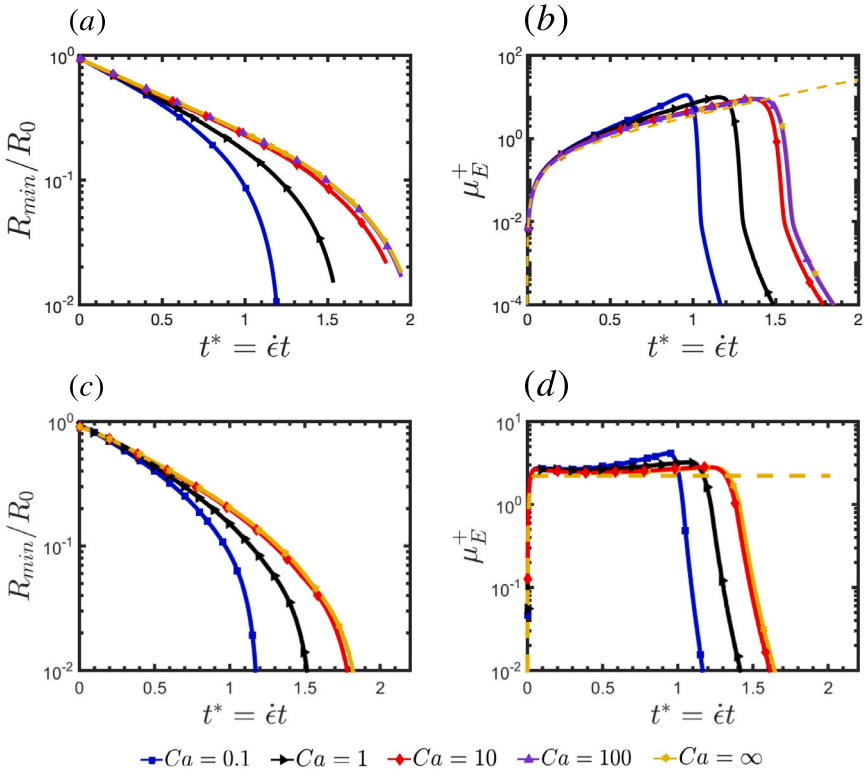

Fig. 8. Normalised width (left column) and extensional viscosity (right column) at the minimum radial section versus the non-dimensional time (or instantaneous extension) t^* for different capillary numbers: $Ca \in [0.1, 1.0, 10, 100, \infty]$ where $Wi = 1.0$, for the figures on the top row and $Wi = 0.01$, for the figures on the bottom one. The other parameters are: $Bi = 1.0$, $Re = 0.01$, $\alpha = 0.5$, $\kappa_\rho = 10^2$ and $\kappa_\mu = 10^4$. The dashed lines represent the analytical solution of Saramito's model where the surface tension is ignored ($Ca = \infty$).

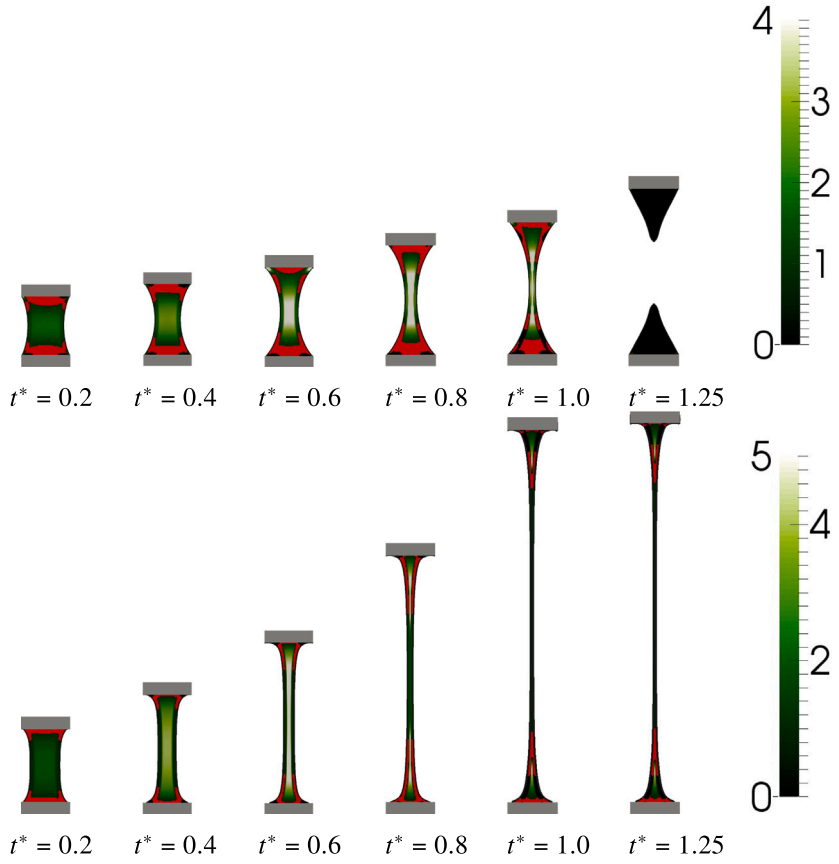

Fig. 9. Visualisation of the EVP sample stretching and evolution of the normal stress difference $[\tau_{11} - \tau_{22}]/\mu_0\dot{\epsilon}$ at $Ca = 0.1$ (top) and $Ca = 100$ (bottom) with $Wi = 1$ for the cases in top row of Fig. 8. The red regions indicate the unyielded material.

so, we consider $Ca \in [0.1, 1, 10, \infty]$, with all the other parameters matching those of the second reference case. Fig. 8(c) and (d) display the normalised width and extensional viscosity for these, essentially viscoplastic, cases. The trend is similar to those discussed above: faster decrease of R_{min}/R_0 and constant value of μ_E over a wide range of time until the width of the material reaches the minimum numerically resolvable. The variations observed when increasing the relative importance of the surface tension are similar to those just discussed for configurations with $Wi = 1$, see panels (a) and (b) of the same figure: the width of the material decreases faster for capillary numbers $Ca \lesssim \mathcal{O}(1)$.

A visualisation of the evolution of the EVP material for two values of the Capillary number ($Ca = 0.1$ and $Ca = 100$) is reported in Fig. 9 for the sample with significant elasticity, $Wi = 1$, where, as before, red regions indicate areas of unyielded material. Unlike the case with low Bi, where unyielded regions appear only at the corners of the endplates, in the low Ca number case, i.e. high surface tension, these regions are first seen at the middle of the endplates and then spread out gradually. This indicates that the high stresses generated by the large interfacial tension forces are primarily concentrated at the midsection (since it is the section with the least width) causing a homogeneous deformation zone [21]. A combination of the homogeneous deformation zone (in the middle of the sample) and the low-stress (unyielded) regions forces the remaining part of the sample to retain its original shape after an initial deformation, while the mid-region undergoes high stresses due to high surface tension. For the high Ca case, i.e. low surface tension, the behaviour is similar to the results for a sample with low Bi number discussed earlier: the unyielded low-stress regions are limited to the areas between the endplates and the interface between the two fluids.

Fig. 10 reports visualisations of the evolution of the material for two values of Capillary number ($Ca = 1$ and $Ca = \infty$) at low elasticity ($Wi = 0.01$) . Similarly to the visualisation for different Capillary numbers at $Wi = 1$ (Fig. 9), we observe that when the surface tension is large ($Ca = 0.1$) the material starts yielding from the centre, where the interfacial stresses are large due to necking and change in the shape of the material, leaving unyielded regions close to the plates. As the extension continues, the width further decreases at the centre, resulting in a larger stress concentration in a narrow region close to the neck. Thus, the unyielded region spreads from the plates towards the centre. Interestingly, comparing the snapshots right before the rupture in the top rows of Figs. 9 and 10, we observe that the material yields at the plates before it reaches the minimum resolvable width when $Wi = 0.01$. This can be understood by considering the fast response of the system at smaller Wi: due to the lack of elasticity, the sample cannot extend more, which leads to a redistribution of the stresses resulting in a decrease in the central part and increase at the endplates.

5.4. Role of the viscosity ratio

We next present results obtained by varying the viscosity ratio. This is defined following [35] as $\alpha = \mu_p/\mu_0$ where $\mu_0 = \mu_1 + \mu_p$ with μ_1 and μ_p the solvent and polymer viscosities. The results obtained with three different values of α are displayed in Fig. 11. First, we observe that the major effect of an increased polymer viscosity, in relation to its solvent counterpart, is to induce an early failure in the extending fluid, the difference being more pronounced when increasing α from 0.5 to 0.9. In particular, we note that for larger value of α, the material produces stronger strain hardening and as a result is in general thicker but reaches its minimum resolvable width earlier [46].

Note also that the values of the extensional viscosity are similar for the cases $\alpha = 0.5$ and $\alpha = 0.9$; in the former case, however, the material fails (reaches the minimum resolvable width) later.

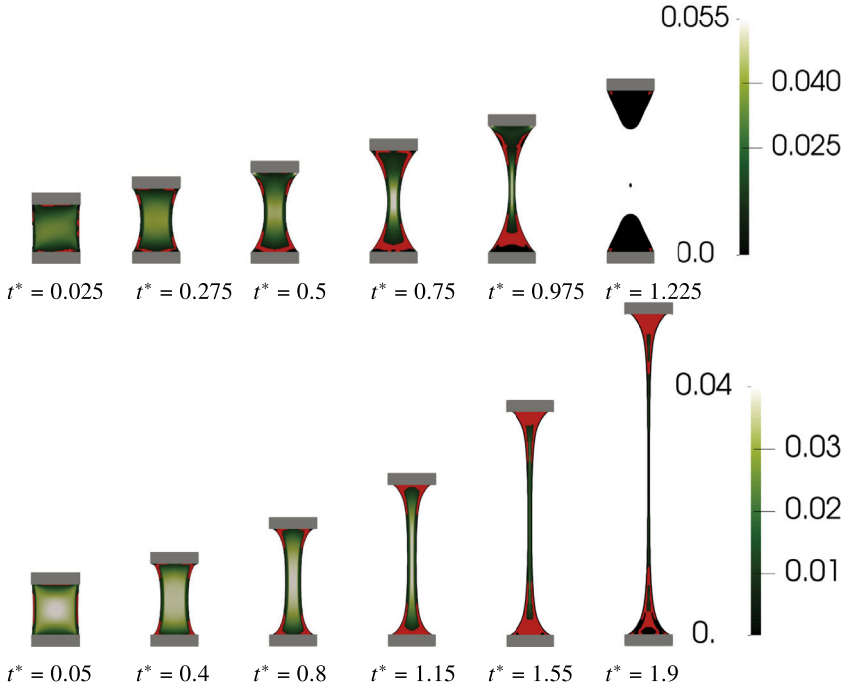

Fig. 10. Visualisation of the EVP sample stretching and evolution of the normal stress difference $\left[\tau_{11} - \tau_{22}\right] / \mu_0 \dot{\epsilon}$ at $Ca = 0.1$ (top) and $Ca = \infty$ (bottom) with $Wi = 0.01$, see also data in bottom row of Fig. 8. The red regions indicate the unyielded material.

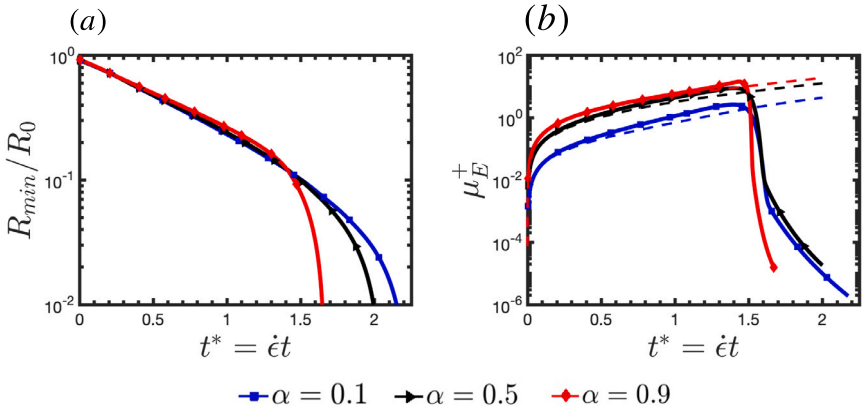

Fig. 11. (a) Normalised width and (b) extensional viscosity at the minimum radial section versus the non-dimensional time (or instantaneous extension) t^* for different viscosity ratios: $\alpha \in [0.1, 0.5, 0.9]$. The other parameters are: $Bi = 1.0, Ca = 100, Re = 0.01, Wi = 1.0, \kappa_p = 10^2$ and $\kappa_\mu = 10^4$. The dashed lines represent the analytical solutions of Saramito's model for the corresponding cases.

A visualisation of the material extension and of the yielded/unyielded regions in the material is displayed in Fig. 12, following the same layout and colour scheme used in the similar figures above. As regards the yielded regions, the extensional stresses are moderate for the viscosity ratio $\alpha = 0.1$ and the behaviour is similar to the cases described earlier with the yielded regions at the corners of the sample, in the regions close to the moving and stationary plate. Conversely, the extensional stresses are larger for the viscosity ratio $\alpha = 0.9$. According to the bottom row of Fig. 12, the stress is higher at the centre of the EVP in the beginning of the extension process, resulting in the formation of unyielded regions on the endplates and at the interface (see the frame at $t^* = 0.4$). The unyielded regions at the endplates gradually reduce as the extension continues, while those at the interface remain (see frames at $t^* = 0.8$ and $t^* = 1.2$). In fact, the interface remains unyielded throughout the extensional process while the thickness of the EVP material reduces. Due to increasing stress concentration in the central part of the necking EVP, the material reaches its minimum resolvable width much earlier than in the two cases with smaller viscosity ratio ($\alpha = 0.1$ and 0.5), which culminates in an abrupt failure of the EVP.

As anticipated in Section 5.2, we present also simulations for the extreme values of the Bingham number (i.e. $Bi = 0.01, 100$) and viscosity ratio (i.e. $\alpha = 0.1, 0.9$), see Fig. 13. For the cases with higher viscosity ratio, the EVP material width decreases faster than for the smaller viscosity ratio (see the left panel of figure) and presents a higher extensional viscosity (see the right panel of Fig. 13).

The visualisation of the extensional dynamics of the cases with smallest Bingham number, $Bi = 0.01$, and $\alpha = 0.1, 0.9$ are reported in Fig. 14. For the smallest value of the viscosity ratio (top row of the figure), the EVP material is completely yielded except for the small regions on the corners attached to the endplates. On the other hand,

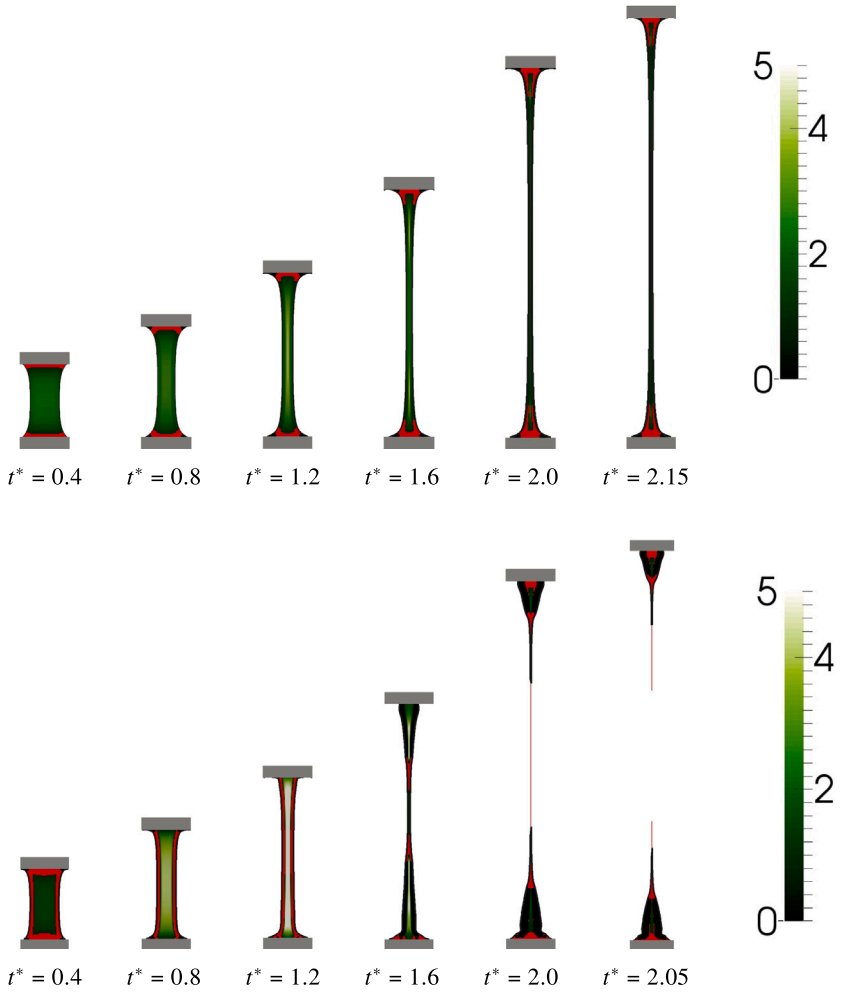

Fig. 12. Visualisation of the EVP sample stretching and evolution of the normal stress difference $\left[\tau_{11} - \tau_{22}\right]/\mu_0\dot{\epsilon}$ at (top) $\alpha = 0.1$ and (bottom) $\alpha = 0.9$ for the cases in Fig. 11. The red regions indicate the unyielded material. The other parameters are: $Bi = 1.0, Ca = 100, Re = 0.01, Wi = 1.0, \kappa_\rho = 10^2$ and $\kappa_\mu = 10^4$.

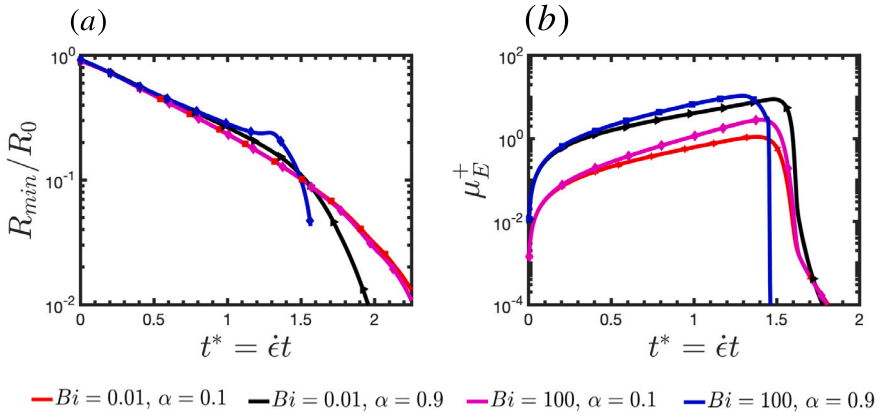

Fig. 13. (a) Normalised width and (b) extensional viscosity at the minimum radial section versus the non-dimensional time (or instantaneous extension) t^* for different yield stress and viscosity ratios. The Bingham number $Bi \in [0.01, 100]$ and viscosity ratio $\alpha \in [0.1, 0.9]$ while the remaining parameters are set to: $Ca = 100, Re = 0.01, Wi = 1.0, \kappa_\rho = 10^2$ and $\kappa_\mu = 10^4$.

for the same Bingham number ($Bi = 0.01$), but higher viscosity ratio ($\alpha = 0.9$), see bottom row of Fig. 14, the unyielded regions on the corner in contact with the endplates grow in size at the interface as the extension progresses. Hence, a high stress region is formed close to the centre of the EVP, away from the solid plates, which accelerates the material rupture.

Finally, Fig. 15 depicts the cases with $Bi = 100$ and $\alpha = 0.1, 0.9$. As expected, since the Bingham number is now large, irrespective of the viscosity ratio, the EVP material remains unyielded throughout the extension process and undergoes elastic solid deformation. For the largest viscosity ratio under consideration (bottom row), the EVP material fails much sooner and attains an asymmetric shape close to the

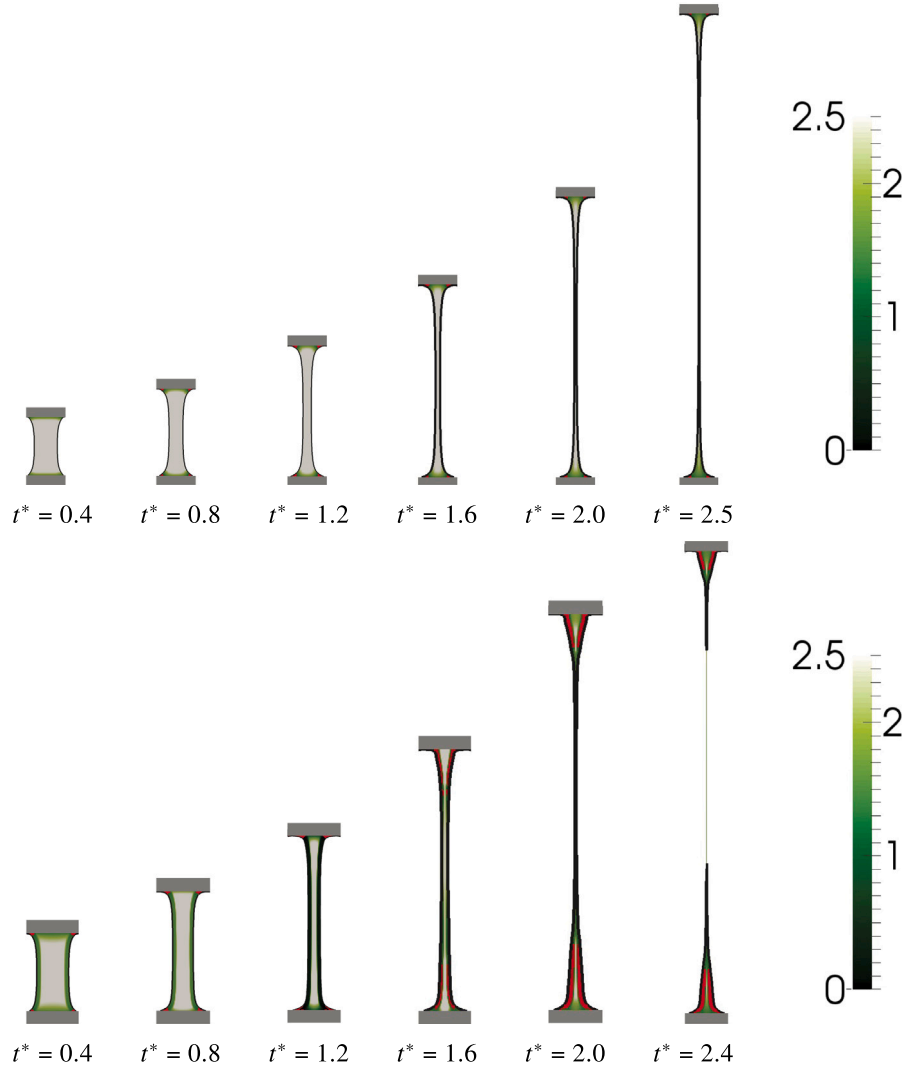

Fig. 14. Visualisation of the EVP sample stretching and evolution of the normal stress difference $\left[\tau_{11} - \tau_{22}\right]/\mu_0\dot{\epsilon}$ at (top) $\alpha = 0.1$ and (bottom) $\alpha = 0.9$ with $Bi = 0.01$ for the cases in Fig. 13. The red regions indicate the unyielded material. The other parameters are: $Ca = 100, Re = 0.01, Wi = 1.0, \kappa_\rho = 10^2$ and $\kappa_\mu = 10^4$.

failure, with the neck located closer to the lower wall. We recall that in our simulations the EVP material is pulled from one side, and for large values of α we observe the material remains solid and the sample follows the upper wall motion more closely. The parts close to the lower wall, instead, are constrained by the no-slip boundary, resulting in a thinner region close to the lower wall where the rupture is observed.

Summarising, the results show that the extensional dynamics is more affected by variations of the viscosity ratio than by variations of the Bingham number when elasticity is an important component of the dynamics. In particular, for larger values of α we observe higher values of the extensional viscosity and the material reaches it minimum resolvable width sooner. This further elucidated the observations in Section 5.2 about the limited role of the Bingham number on the extension of the EVP material for small values of the viscosity ratio. Indeed, the failure is similar for different values of Bi when $\alpha \lesssim 0.5$ and occurs nearly at the same time; this is because the dynamics of a Kelvin–Voigt solid and Oldroyd-B viscoelastic fluid are similar for low viscosity ratios (similar material viscosity in yielded and unyielded conditions) although the stresses experienced by the sample (due to varying Bingham number) differ.

6. Conclusions

The extensional dynamics of an elasto-viscoplastic (EVP) fluid is studied by means of a novel numerical setup, closely modelling an experimental extensional configuration. Specifically, we track the interface between the EVP material and the Newtonian medium using an algebraic volume of fluid method (MTHINC-VOF) and employ a fully Eulerian immersed boundary method (IBM) to model the motion of the piston responsible of the extension of the material. The constitutive model proposed by Saramito [7] is used to compute the non-Newtonian stresses in the EVP material.

We investigate the role of the yield stress threshold, the surface tension coefficient, the viscosity ratio, and the extension rate on the dynamics of the EVP material by separately changing the Bingham number ($Bi = 0, 0.01, 1, 100$), capillary number ($Ca = 0.1, 1, 10, 100$), viscosity ratio ($\alpha = 0.1, 0.5, 0.9$), and Weissenberg number ($Wi = 0.1, 1, 10$) with respect to two reference configurations with $Bi = 1, Ca = 100, \alpha = 0.5$, and $Wi = 1$ and $Wi = 0.01$. To quantify the differences in the extensional dynamics, we report the minimum thickness of the EVP sample and its extensional viscosity for each case under consideration. Visualisations are used to highlight the yielded and unyielded regions of the material during the extension and before the minimum resolvable width is obtained.

First, our results demonstrate that for small values of Wi, i.e., approaching the limit of a viscoplastic material, when the polymer relaxation is faster than the imposed extension rate, the extensional viscosity reaches a steady state value before the final failure of the EVP material. Conversely, for large Wi, the extensional viscosity increases

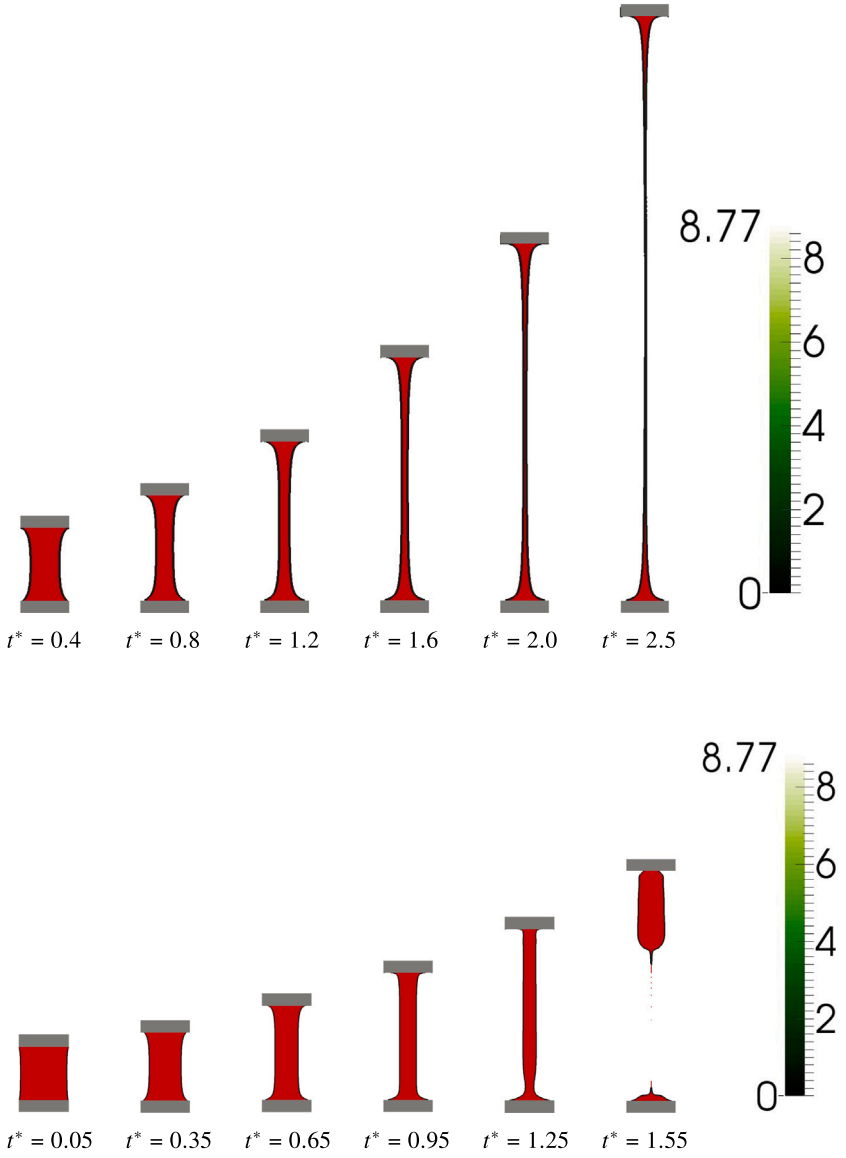

Fig. 15. Visualisation of the EVP sample stretching and evolution of the normal stress difference $\left[\tau_{11} - \tau_{22}\right] / \mu_0 \dot{\epsilon}$ at (top) $\alpha = 0.1$ and (bottom) $\alpha = 0.9$ with $Bi = 100$ for the cases in Fig. 13. The red regions indicate the unyielded material. The other parameters are: $Ca = 100, Re = 0.01, Wi = 1.0, \kappa_\rho = 10^2$ and $\kappa_\mu = 10^4$.

continuously until the EVP material breaks. For small Wi, the slower extension results in lower shear and extensional stresses which explains the presence of large unyielded regions close to the endplates. On the other hand, the presence of relatively large unyielded regions in case of high Wi is due to the fast exponential dynamics (slower material response). We believe that these regions are just remaining from the initial state given the slow material response.

The results of our simulation reveal that the extensional dynamics undergoes minor variations when changing the Bingham number Bi at fixed viscosity ratio $\alpha = 0.5$, although the yield stress varies by several orders of magnitude when the material elasticity is important. We observe that for the largest values of Bi, the EVP material behaves as an elastic solid, whereas at lower values the yielding starts from the middle of the EVP sample and extends towards the end plates forming pockets of unyielded elastic solid close to the edges of the end plates. The small differences are explained by the similar magnitude of viscosity and elasticity of the yielded and unyielded phases. On the other hand, we observe an increase of the extensional viscosity with Bi in the limit of a viscoplastic material. Also, at low elasticity, the material response is fast and the extensional viscosity attains a plateau before the material reaches its minimum width.

An important observation is that the EVP reaches the minimum resolvable width faster for lower values of the capillary number, $Ca \approx \mathcal{O}(1)$, and that neglecting the surface tension forces results in inaccurate predictions of the dynamics especially when the extension rate is relatively slow. In addition to the dynamics of the sample under extension, the simulation results illustrate the importance of the surface tension coefficient in the yielding process; for small values of Ca, the unyielded regions first appear at the middle of the endplates, followed by a gradual spreading towards the interface. In other words, due to the large interfacial tension at the midsection of the sample (the section with the least width of curvature), the EVP first yields in this region while it is still unyielded at the endplates. On the other hand, for large values of Ca, the unyielded regions appear only at the corners of the endplates.

By examining the role of the viscosity ratio, we conclude that due to stronger strain hardening effects, the EVP material remains thicker for larger values of α and fails sooner. As regards the yielded region, for small values of viscosity ratio, the sample first yields everywhere but at the endplates then, as the extension process continues, the corners of the sample at the solid substrate and on the piston yield as well and only the region close to the centre of the endplates remains unyielded.

On the other hand, for large values of viscosity ratio, the EVP fluid yields only in the central part of the sample in the beginning of the extension process, while remaining unyielded both at the interface and the endplates.

We believe that the numerical framework introduced here can be used for high-fidelity simulations of EVP materials to test different constitutive relations against experimental data. The flexibility of the setup provides the possibility to change the material constitutive equations and perform numerical simulations for a variety of non-Newtonian models.

Declaration of competing interest

The authors declare that they have no known competing financial interests or personal relationships that could have appeared to influence the work reported in this paper.

Data availability

Data will be made available on request

Acknowledgements

The authors wish to thank Prof. Randy H. Ewoldt for fruitful discussions. Muhammed Abdulrazaq is particularly thankful for the time spent at the Mechanical Engineering Laboratory in University of Illinois at Urbana-Champaign, which initiated and inspired this work. The research was supported by the Swedish Research Council, via the multidisciplinary research environment INTERFACE (VR 2016–06119 "Hybrid multiscale modelling of transport phenomena for energy efficient processes"). The computation resources were provided by SNIC (Swedish National Infrastructure for Computing) and by the National Infrastructure for High Performance Computing and Data Storage in Norway (project no. NN9561K). MER was supported by the Okinawa Institute of Science and Technology Graduate University, Japan (OIST) with subsidy funding from the Cabinet Office, Government of Japan and by the JSPS KAKENHI Grant Number JP20K22402.

References

[1] P. Saramito, Complex Fluids, Springer, 2016.
[2] A.Z. Nelson, R.E. Bras, J. Liu, R.H. Ewoldt, Extending yield-stress fluid paradigms, J. Rheol. 62 (1) (2018) 357–369.
[3] G.H. McKinley, O. Hassager, The considere condition and rapid stretching of linear and branched polymer melts, J. Rheol. 43 (5) (1999) 1195–1212.
[4] S.M. Fielding, Criterion for extensional necking instability in polymeric fluids, Phys. Rev. Lett. 107 (25) (2011) 258301.
[5] G.H. McKinley, Visco-elasto-capillary thinning and break-up of complex fluids, 2005.
[6] C. Dimitriou, The Rheological Complexity of Waxy Crude Oils: Yielding, Thixotropy and Shear Heterogeneities (Ph.D. thesis), Massachusetts Institute of Technology, 2013.
[7] P. Saramito, A new constitutive equation for elastoviscoplastic fluid flows, J. Non-Newton. Fluid Mech. 145 (1) (2007) 1–14.
[8] J.-M. Piau, Carbopol gels: Elastoviscoplastic and slippery glasses made of individual swollen sponges: Meso-and macroscopic properties, constitutive equations and scaling laws, J. Non-Newton. Fluid Mech. 144 (1) (2007) 1–29.
[9] N.J. Balmforth, N. Dubash, A.C. Slim, Extensional dynamics of viscoplastic filaments: II. Drips and bridges, J. Non-Newton. Fluid Mech. 165 (19–20) (2010) 1147–1160.
[10] Y. Holenberg, O.M. Lavrenteva, U. Shavit, A. Nir, Particle tracking velocimetry and particle image velocimetry study of the slow motion of rough and smooth solid spheres in a yield-stress fluid, Phys. Rev. E 86 (6) (2012) 066301.
[11] A.S. Yoshimura, R.K. Prud'homme, Response of an elastic bingham fluid to oscillatory shear, Rheol. Acta 26 (5) (1987) 428–436.
[12] D. Doraiswamy, A. Mujumdar, I. Tsao, A. Beris, S. Danforth, A. Metzner, The Cox–Merz rule extended: A rheological model for concentrated suspensions and other materials with a yield stress, J. Rheol. 35 (4) (1991) 647–685.
[13] P. Sollich, Rheological constitutive equation for a model of soft glassy materials, Phys. Rev. E 58 (1) (1998) 738.
[14] G. Katgert, M.E. Möbius, M. van Hecke, Rate dependence and role of disorder in linearly sheared two-dimensional foams, Phys. Rev. Lett. 101 (5) (2008) 058301.
[15] P. Saramito, A new elastoviscoplastic model based on the Herschel–Bulkley viscoplastic model, J. Non-Newton. Fluid Mech. 158 (1–3) (2009) 154–161.
[16] S. Bénito, C.-H. Bruneau, T. Colin, C. Gay, F. Molino, An elasto-visco-plastic model for immortal foams or emulsions, Eur. Phys. J. E 25 (3) (2008) 225–251.
[17] C.J. Dimitriou, G.H. McKinley, A canonical framework for modeling elasto-viscoplasticity in complex fluids, J. Non-Newton. Fluid Mech. 265 (2019) 116–132.
[18] M. Rosti, D. Izbassarov, O. Tammisola, S. Hormozi, L. Brandt, Turbulent channel flow of an elastoviscoplastic fluid, J. Fluid Mech. 853 (2018) 488–514, http://dx.doi.org/10.1017/jfm.2018.591, URL https://www.sciencedirect.com/science/article/pii/S0377025707000869.
[19] F. De Vita, M. Rosti, D. Izbassarov, L. Duffo, O. Tammisola, S. Hormozi, L. Brandt, Elastoviscoplastic flows in porous media, J. Non-Newton. Fluid Mech. 258 (2018) 10–21, http://dx.doi.org/10.1016/j.jnnfm.2018.04.006, URL https://www.sciencedirect.com/science/article/pii/S0377025718300223.
[20] S. Le Clainche, D. Izbassarov, M. Rosti, L. Brandt, O. Tammisola, Coherent structures in the turbulent channel flow of an elastoviscoplastic fluid, J. Fluid Mech. 888 (2020) A5, http://dx.doi.org/10.1017/jfm.2020.31.
[21] M. Yao, G.H. McKinley, Numerical simulation of extensional deformations of viscoelastic liquid bridges in filament stretching devices, J. Non-Newton. Fluid Mech. 74 (1–3) (1998) 47–88.
[22] G.H. McKinley, T. Sridhar, Filament-stretching rheometry of complex fluids, Annu. Rev. Fluid Mech. 34 (1) (2002) 375–415.
[23] R. Valette, E. Hachem, M. Khalloufi, A.S. Pereira, M. Mackley, S. Butler, The effect of viscosity, yield stress, and surface tension on the deformation and breakup profiles of fluid filaments stretched at very high velocities, J. Non-Newton. Fluid Mech. 263 (2019) 130–139.
[24] D.M. Hoyle, S.M. Fielding, Criteria for extensional necking instability in complex fluids and soft solids. Part I: Imposed Hencky strain rate protocol, J. Rheol. 60 (6) (2016) 1347–1375.
[25] D.M. Hoyle, S.M. Fielding, Criteria for extensional necking instability in complex fluids and soft solids. Part II: Imposed tensile stress and force protocols, J. Rheol. 60 (6) (2016) 1377–1397.
[26] R. Sizaire, V. Legat, Finite element simulation of a filament stretching extensional rheometer, J. Non-Newton. Fluid Mech. 71 (1–2) (1997) 89–107.
[27] M.I. Kolte, H.K. Rasmussen, O. Hassager, Transient filament stretching rheometer, Rheol. Acta 36 (3) (1997) 285–302.
[28] S. Gaudet, G.H. McKinley, Extensional deformation of non-Newtonian liquid bridges, Comput. Mech. 21 (6) (1998) 461–476.
[29] A. Shahmardi, M.E. Rosti, O. Tammisola, L. Brandt, A fully Eulerian hybrid immersed boundary-phase field model for contact line dynamics on complex geometries, J. Comput. Phys. 443 (2021) 110468, http://dx.doi.org/10.1016/j.jcp.2021.110468, URL https://www.sciencedirect.com/science/article/pii/S0021999121003636.
[30] Y. Dimakopoulos, G. Makrigiorgos, G.C. Georgiou, J. Tsamopoulos, The PAL (Penalized Augmented Lagrangian) method for computing viscoplastic flows: A new fast converging scheme, J. Non-Newton. Fluid Mech. 256 (2018) 23–41.
[31] P. Moschopoulos, A. Syrakos, Y. Dimakopoulos, J. Tsamopoulos, Dynamics of viscoplastic filament stretching, J. Non-Newton. Fluid Mech. 284 (2020) 104371.
[32] D. Izbassarov, M.E. Rosti, M.N. Ardekani, M. Sarabian, S. Hormozi, L. Brandt, O. Tammisola, Computational modeling of multiphase viscoelastic and elastoviscoplastic flows, Internat. J. Numer. Methods Fluids 88 (12) (2018) 521–543.
[33] M. Alves, P. Oliveira, F. Pinho, Numerical methods for viscoelastic fluid flows, Annu. Rev. Fluid Mech. 53 (2021) 509–541.
[34] S. Ii, K. Sugiyama, S. Takeuchi, S. Takagi, Y. Matsumoto, F. Xiao, An interface capturing method with a continuous function: The THINC method with multi-dimensional reconstruction, J. Comput. Phys. 231 (5) (2012) 2328–2358, http://dx.doi.org/10.1016/j.jcp.2011.11.038, URL https://www.sciencedirect.com/science/article/pii/S0021999111006942.
[35] P. Saramito, A new constitutive equation for elastoviscoplastic fluid flows, J. Non-Newton. Fluid Mech. 145 (1) (2007) 1–14, http://dx.doi.org/10.1016/j.jnnfm.2007.04.004, URL https://www.sciencedirect.com/science/article/pii/S0377025707000869.
[36] M.S. Dodd, A. Ferrante, A fast pressure-correction method for incompressible two-fluid flows, J. Comput. Phys. 273 (2014) 416–434.
[37] S. Li, K. Sugiyama, S. Takeuchi, Y. Matsumoto, F. Xiao, An interface capturing method with a continuous function: The THINC method with multi-dimensional reconstruction, J. Comput. Phys. 231 (2012) 2328–2358, http://dx.doi.org/10.1016/j.jcp.2011.11.038.
[38] M.E. Rosti, F.D. Vita, L. Brandt, Numerical simulations of emulsions in shear flows, Acta Mech. 230 (2018) 667–682, http://dx.doi.org/10.1007/s00707-018-2265-5.
[39] J. Brackbill, D. Kothe, C. Zemach, A continuum method for modeling surface tension, J. Comput. Phys. 100 (2) (1992) 335–354, http://dx.doi.org/10.1016/0021-9991(92)90240-Y, URL https://www.sciencedirect.com/science/article/pii/002199919290240Y.
[40] T. Kajishima, T. Satoshi, H. HAMASAKI, Y. MIYAKE, Turbulence structure of particle-laden flow in a vertical plane channel due to vortex shedding, JSME Int. J. Ser. B Fluids Therm. Eng. 44 (2001) 526–535, http://dx.doi.org/10.1299/jsmeb.44.526.

[41] F. De Vita, M.E. Rosti, D. Izbassarov, L. Duffo, O. Tammisola, S. Hormozi, L. Brandt, Elastoviscoplastic flows in porous media, J. Non-Newton. Fluid Mech. 258 (2018) 10–21.
[42] L.E. Rodd, T.P. Scott, J.J. Cooper-White, G.H. McKinley, Capillary break-up rheometry of low-viscosity elastic fluids, Appl. Rheol. 15 (1) (2005) 12–27.
[43] D.O. Olagunju, A 1-D theory for extensional deformation of a viscoelastic filament under exponential stretching, J. Non-Newton. Fluid Mech. 87 (1) (1999) 27–46.
[44] V. Entov, E. Hinch, Effect of a spectrum of relaxation times on the capillary thinning of a filament of elastic liquid, J. Non-Newton. Fluid Mech. 72 (1) (1997) 31–53.
[45] P. Szabo, Transient filament stretching rheometer, Rheol. Acta 36 (3) (1997) 277–284.
[46] P.P. Bhat, M. Pasquali, O.A. Basaran, Beads-on-string formation during filament pinch-off: Dynamics with the PTT model for non-affine motion, J. Non-Newton. Fluid Mech. 159 (1–3) (2009) 64–71.